

Focusing of elastic waves for microseismic imaging

Johannes Douma and Roel Snieder

Center for Wave Phenomena, Colorado School of Mines, Golden, CO 80401, USA. E-mail: jdouma1992@gmail.com

Accepted 2014 October 13. Received 2014 October 10; in original form 2013 December 18

SUMMARY

Microseismic events generate compressive waves and shear waves, which can be recorded at receivers. We present a theory that shows how elastic P and S waves separately backpropagate to the original source location. These refocused P and S wavefields are free of singularities. We also demonstrate a technique that enhances the ability to image the spatial focus for each wave type using elastic waves. The improved spatial focus obtained is achieved in a velocity model for which the interface boundaries are approximate but where the mean slowness is correct. Deconvolution designs a signal to be rebroadcasted from the receivers, using only the waves recorded at each receiver, such that the wavefield has an optimal temporal focus at the source location. We demonstrate theoretically and numerically that improved temporal focusing of elastic waves leads to improved spatial focusing for each wave type. This proposed technique only involves a simple pre-processing step to the recorded data and its cost is hence negligible compared to the total cost of microseismic imaging.

Key words: Image processing; Fourier analysis; Earthquake source observations; Computational seismology; Fractures and faults.

INTRODUCTION

Due to hydraulic fracturing becoming a common practice for unconventional gas and oil fields, there has been an increased interest into the study of microseismic events. Clusters of microseismic events delineate faults and the formation of fractures, and can indicate new or reactivating regions of failure. These microseismic events can be generated naturally or as a result of hydraulic stimulation (Duncan 2005; Kendall *et al.* 2011). Therefore, the petroleum industry desires to develop more accurate ways of locating, and monitoring microseismic events to potentially improve their relationship to production and completion data (Foulger & Julian 2012).

A common processing method to locate microseismic events or earthquakes is based on picking arrival times of the acoustic and shear waves. This process, however, is difficult to do accurately when significant noise is present in the data (Bose *et al.* 2009; Bancroft *et al.* 2010; Kummerow 2010; Song *et al.* 2010; Hayles *et al.* 2011). An alternative approach, which requires less user interaction and allows for more accuracy, is using time reversal to image the focus of the microseismic events or earthquakes at the source location (Larmat *et al.* 2006, 2010; Lu 2008; Steiner *et al.* 2008; Lu & Willis 2008; Artman *et al.* 2010). In this imaging approach, one uses time reversal to focus the recorded signal at the source location in both time and space. The advantage of time reversal is that it does not require picking of arrival times which is important when dealing with noisy data.

If one would time reverse the waves at every point in space, the wavefield will focus onto the original source location. If, however,

the wavefield is sampled at only a limited number of locations, then it is not obvious that time reversal is the optimal way to focus energy on the original source. Much research has been carried out on focusing sparsely sampled wavefields (Parvulescu 1961; Fink 1997; Roux & Fink 2000; Tanter *et al.* 2000, 2001; Aubry *et al.* 2001; Bertaix *et al.* 2004; Jonsson *et al.* 2004; Montaldo *et al.* 2004; Vignon *et al.* 2006; Larmat *et al.* 2010; Gallot *et al.* 2011). In this paper, we explore a simple extension to time reversal, based on deconvolution, as previously derived by Anderson *et al.* (2014). We have shown earlier that deconvolution improves the locating of microseismic events in an acoustic medium (Douma *et al.* 2013). We now demonstrate deconvolution's ability to improve the imaging of a microseismic event in an elastic medium. This method is a robust, though simplified, version of the inverse filter (Tanter *et al.* 2000, 2001; Gallot *et al.* 2011). It calculates a signal to be rebroadcast from the receiver such that the output at the focal location becomes an approximate delta function $\delta(t)$ and uses only the recorded signals at each receiver.

As with all imaging methods, reverse time imaging is unable to locate the microseismic event to a point location when the velocity model used for the backpropagation differs from the true velocity model, or when the aperture is limited; it causes the spatial image to defocus. In the numerical example used for this paper, the aperture used is not perfect, thus, the wavefield is not known at every point in both time and space. Additionally, we complicate our model by adding noise and backpropagating our wavefields not through the correct velocity model but through a smoothed version of the velocity model.

In this paper, we first derive a relationship between the temporal focus and the incoming wave for an elastic medium. The theory is used to show that improved temporal focusing leads to improved spatial focusing for each wave type due to different sources (explosive, point force and double couple). We then show a numerical example in which a horizontal point force excites elastic waves.

THEORY

In this section, we show that improved temporal focusing leads to improved spatial focusing for both P and S waves. Just as in the theory for the excitation of elastic waves (Aki & Richards 2002), we treat the medium as locally homogeneous near the focus. The complexity of the wavefield due to heterogeneity is captured in the wave that is incident on the focus. We thus consider a locally homogeneous elastic medium where either P , SV or SH waves are incident on a focal point. According to expression (8.13) of Aki & Richards (2002), the elastic wavefield can locally be expressed as

$$\mathbf{u}(r, \theta, \varphi) = \sum_{lm} (U_l(r) \mathbf{R}_l^m(\theta, \varphi) + V_l(r) \mathbf{S}_l^m(\theta, \varphi) + W_l(r) \mathbf{T}_l^m(\theta, \varphi)). \quad (1)$$

The vector spherical harmonics in eq. (1) are given by

$$\mathbf{R}_l^m(\theta, \varphi) = Y_{lm}(\theta, \varphi) \hat{\mathbf{r}} \quad (P \text{ waves}), \quad (2)$$

$$\mathbf{S}_l^m(\theta, \varphi) = \frac{1}{\sqrt{l(l+1)}} \left(\frac{\partial Y_{lm}(\theta, \varphi)}{\partial \theta} \hat{\theta} + \frac{1}{\sin \theta} \frac{\partial Y_{lm}(\theta, \varphi)}{\partial \varphi} \hat{\varphi} \right) \quad (SV \text{ waves}), \quad (3)$$

$$\mathbf{T}_l^m(\theta, \varphi) = \frac{1}{\sqrt{l(l+1)}} \left(\frac{1}{\sin \theta} \frac{\partial Y_{lm}(\theta, \varphi)}{\partial \varphi} \hat{\theta} - \frac{\partial Y_{lm}(\theta, \varphi)}{\partial \theta} \hat{\varphi} \right) \quad (SH \text{ waves}), \quad (4)$$

where $Y_{lm}(\theta, \varphi)$ denote the spherical harmonics. The radial functions $U_l(r)$, $V_l(r)$ and $W_l(r)$ are spherical Bessel functions or spherical Hankel functions which satisfy eq. (8.6) of Aki & Richards (2002). We stress that the vector spherical harmonics of expressions (2)–(4) do not denote the normal modes of a finite system, instead they are representations of the wavefield in a locally homogeneous medium.

We consider the case of an incoming wave that, at a large distance from the focal point $\mathbf{r} = 0$, is given by $f_l(t + r/c)/r$. We study the properties of this incoming wave at the focus for every angular degree l separately. For a perfect aperture, the angular degree l describes an explosive source when $l = 0$, a point force when $l = 1$ and a double-couple source when $l = 2$. Since there is no source at the location $\mathbf{r} = 0$, the solution is finite and is therefore given by spherical Hankel functions j_l :

$$U_l(r) \propto j_l(kr) \quad \text{where} \quad k = \omega/\alpha, \quad (5)$$

with α representing the P -wave velocity, and

$$V_l(r) \quad \text{and} \quad W_l(r) \propto j_l(kr) \quad \text{with} \quad k = \omega/\beta, \quad (6)$$

where β is the S -wave velocity. Thus, the radial variation of the wavefield is proportional to $j_l(kr)$, with k the wavenumber of the wave type under consideration. In the following, we study wavefields with radial dependence $j_l(kr)$ and denote the wavenumber as

$$k = \omega/c, \quad (7)$$

where c is the appropriate wave velocity (α or β depending on the wave type). It is understood that the total wavefield follows by multiplying with the appropriate vector spherical harmonic as given in expressions (2)–(4). The radial dependence of the wavefield in the frequency domain, therefore, is given by

$$U_l(r, \omega) = A_l(\omega) j_l(kr), \quad (8)$$

where $A_l(\omega)$ is a Fourier coefficient.

Using the Fourier convention $f(t) = \int F(\omega) e^{-i\omega t} d\omega$, the wavefield in the time domain is given by

$$u_l(r, t) = \int A_l(\omega) j_l(kr) e^{-i\omega t} d\omega. \quad (9)$$

The waves impinging on the focus are determined by the incoming waves. For large radius r , the incoming waves can be written as

$$u_l^{\text{inc}}(r, t) = \frac{f_l(t + r/c)}{r} \quad \text{as} \quad r \rightarrow \infty. \quad (10)$$

We show in the Appendix that the total wavefield is given for all values of r by,

$$u_l(r, t) = (-i)^l \frac{2}{c} \int (-i\omega) F_l(\omega) j_l(kr) e^{-i\omega t} d\omega, \quad (11)$$

where $F_l(\omega)$ is the Fourier transform of $f_l(t)$.

Because our derivation involves repeated differentiations and integrations, we employ the following notation:

$$f_l^{(n)}(t) \equiv \frac{d^n f_l(t)}{dt^n}. \quad (12)$$

For negative values of n , this notation implies integrating $f_l(t)$ n times. In the frequency domain, the notation (12) translates into

$$F_l^{(n)}(\omega) \equiv (-i\omega)^n F_l(\omega). \quad (13)$$

Next, we relate the total wavefield $u_l(r, t)$ to the spherical Bessel function of order 0 which makes it possible to evaluate the Fourier integral in eq. (11) analytically. This derivation, found in the Appendix, gives:

$$u_l(r, t) = c^l r^l \left(\frac{1}{r} \frac{d}{dr} \right)^l \left(\frac{f_l^{(-l)}(t + r/c) - f_l^{(-l)}(t - r/c)}{r} \right). \quad (14)$$

This expression shows an explicit relationship between the total wavefield $u_l(r, t)$ for all values of r , and the incident wave, $f_l(t + r/c)/r$ at a distance. Note that using the notation of eqs (12) and (13), the incoming wave is integrated l times in the factor $f_l^{(-l)}(t \pm r/c)$, and that the differential operator $(1/r)(d/dr)$ acts l times as well. The term $f_l^{(-l)}(t + r/c)$ is the wave that converges on the focal point, while $f_l^{(-l)}(t - r/c)$ gives the outgoing wave that radiates from the focus after the incoming waves have passed through that point. The incident wave $f_l(t + r/c)$ and the outgoing wave $f_l(t - r/c)$ have opposite sign because the focus is a caustic in two angular directions, hence the Maslow index increases by two, which corresponds to a sign change (Chapman 2004). Note that a point source is, by definition, located at a caustic of the excited or backpropagated wavefield. The theory presented takes this fully into account.

We now demonstrate how we can use the expression for the wavefield near the focal point to demonstrate that improved temporal focusing leads to improved spatial focusing. The spatial focus $R_l(r)$ is defined as the wavefield at time $t = 0$. It follows from expression

(14) that the spatial focus is given by:

$$R_l(r) \equiv u_l(r, t = 0) = c^l r^l \left(\frac{1}{r} \frac{d}{dr} \right)^l \left(\frac{f_l^{(-l)}(r/c) - f_l^{(-l)}(-r/c)}{r} \right). \quad (15)$$

This expression gives the spatial focus in terms of the incoming wave.

One might be tempted to define the temporal focus as $u_l(r = 0, t)$. This field, according to expression (9), is proportional to $j_l(kr)$ in the frequency domain. The zeroth-order Bessel function $j_0(kr)$ is non-zero for $r = 0$, but $j_l(kr) = 0$ for $l \geq 1$ (Arfken & Weber 2001). This means that for $l \geq 1$, the wavefield vanishes at the focal point. Physically, this is due to the fact that for $l \geq 1$, the focal point ($r = 0$) is located at the intersection of nodal lines. Since $U_l(r = 0, t)$ vanishes at $r = 0$ for $l \geq 1$, this quantity is not a useful diagnostic of the temporal focus. To remedy this, we define the temporal focus instead as

$$T_l(t) \equiv \frac{d^l}{dt^l} u_l(r = 0, t). \quad (16)$$

As shown in the Appendix, the l -th derivative of $j_l(kr)$ is finite and non-zero for $r = 0$. We derive in the Appendix the following relation between the temporal focus and the incoming waves:

$$T_l(t) = \frac{2b_l}{c^{l+1}} f_l^{(l+1)}(t), \quad (17)$$

where b_l is given by

$$b_l = \frac{2^l (l!)^2}{(2l + 1)!}. \quad (18)$$

Specifically,

$$b_0 = 1, \quad b_1 = 1/3, \quad b_2 = 2/15.$$

According to eq. (17), the temporal focus thus is proportional to the $(l + 1)$ -th time derivative of the incoming wave. Of these $(l + 1)$ derivatives, given by eq. (17), l are due to the derivatives in definition (16). One time derivative is due to the fact that (14) contains the combination $(f_l(t + r/c) - f_l(t - r/c))/r$. Using a Taylor expansion and taking the limit $r \rightarrow 0$, gives

$$\lim_{r \rightarrow 0} \frac{f_l(t + r/c) - f_l(t - r/c)}{r} = \lim_{r \rightarrow 0} \frac{2(r/c) f_l'(t)}{r} = \frac{2}{c} f_l'(t).$$

This explains an additional time derivative in expression (17).

SPATIAL AND TEMPORAL FOCUS FOR EACH ANGULAR COMPONENT

The spatial and temporal focus defined by expressions (15) and (17) both relate to the incoming waves and can be combined to explicitly relate the spatial and temporal focus:

$$R_l(r) = \frac{c^{2l+1}}{2b_l} r^l \left(\frac{1}{r} \frac{d}{dr} \right)^l \left(\frac{T_l^{(-2l-1)}(r/c) - T_l^{(-2l-1)}(-r/c)}{r} \right). \quad (19)$$

Eq. (19) is the main result of the theory. Although the relation (19) between the spatial and temporal focus is complicated, it does show that good temporal focusing implies good spatial focusing. Good temporal focusing implies that $T_l(t)$ is strongly peaked near $t = 0$, that is, that $T_l(t)$ only differs appreciably from zero for a small

range of time values $-t_f < t < t_f$, where t_f is the half width of the temporal focus. Expression (19) implies that the spatial focus differs appreciably from zero for values of r that satisfy $0 \leq r < ct_f$ (radius is always positive). A good temporal focus (small t_f) thus implies a good spatial focus.

The spatial and temporal focus, and their relationship defined by eqs (15), (17) and (19) all depend on the order l . In this section, we show the explicit forms of these expressions for the case $l = 0$, $l = 1$ and $l = 2$. These cases are relevant for an explosive source ($l = 0$), point force ($l = 1$) and double-couple source ($l = 2$) if the aperture would be perfect. For $l = 0$, eqs (15), (17) and (19) become, respectively,

$$R_0(r) = \left(\frac{f_0(r/c) - f_0(-r/c)}{r} \right), \quad (20)$$

$$T_0(t) = \frac{2}{c} f_0^{(1)}(t) \quad \text{and} \quad (21)$$

$$R_0(r) = \frac{c}{2} \left(\frac{T_0^{(-1)}(r/c) - T_0^{(-1)}(-r/c)}{r} \right). \quad (22)$$

Eqs (20)–(22) are the same as shown in the previous derivation of Anderson *et al.* (2014), which dealt with an explosive source in an acoustic medium where the temporal focus is the time derivative of the incoming wave.

We now continue the derivation for $R(r)$ due to a point force ($l = 1$) and double-couple ($l = 2$). For $l = 1$, eqs (15), (17) and (19) become, respectively,

$$R_1(r) = \frac{1}{r} (f_1(r/c) + f_1(-r/c)) - \frac{c}{r^2} (f_1^{(-1)}(r/c) - f_1^{(-1)}(-r/c)), \quad (23)$$

$$T_1(t) = \frac{3}{2c^2} f_1^{(2)}(t) \quad \text{and} \quad (24)$$

$$R_1(r) = \frac{2c^2}{3} \frac{1}{r} (T_1^{(-2)}(r/c) + T_1^{(-2)}(-r/c)) - \frac{2c^3}{3} \frac{1}{r^2} (T_1^{(-3)}(r/c) - T_1^{(-3)}(-r/c)). \quad (25)$$

It may appear that eq. (23) is singular at $r = 0$. Even though each of the two terms in this expression diverge as $r \rightarrow 0$, the singularities cancel. This can be verified by writing $f_1(r/c) = a_0 + O(r)$. Integrating this once gives $f_1^{(-1)}(r/c) = a_0(r/c) + O(r^2)$. Inserting this into eq. (23) gives

$$R_1(r) = \frac{1}{r} (2a_0 + O(r)) - \frac{c}{r^2} (2a_0(r/c) + O(r^2)). \quad (26)$$

The terms proportional to a_0 , which caused each of the individual terms in expression (23) to be singular, cancel out. The remainder of eq. (26) is finite as $r \rightarrow 0$.

For $l = 2$, eqs (15), (17) and (19) become, respectively,

$$R_2(r) = \frac{1}{r} (f_2(r/c) - f_2(-r/c)) - \frac{3c}{r^2} (f_2^{(-1)}(r/c) + f_2^{(-1)}(-r/c)) + \frac{3c^2}{r^3} (f_2^{(-2)}(r/c) - f_2^{(-2)}(-r/c)), \quad (27)$$

$$T_2(t) = \frac{4}{15c^3} f_2^{(3)}(t) \quad \text{and} \quad (28)$$

$$\begin{aligned}
R_2(r) = & \frac{15c^3}{4} \frac{1}{r} \left(T_2^{(-3)}(r/c) - T_2^{(-3)}(-r/c) \right) \\
& - \frac{45c^4}{4} \frac{1}{r^2} \left(T_1^{(-4)}(r/c) + T_1^{(-4)}(-r/c) \right) \\
& + \frac{45c^5}{4} \frac{1}{r^3} \left(T_1^{(-5)}(r/c) - T_1^{(-5)}(-r/c) \right). \quad (29)
\end{aligned}$$

The wavefields computed are finite at the focal point $r = 0$ when one refocuses either P or S waves. In contrast, when P and S waves are excited by a point force, the P -wave component and the S -wave component behave as $1/r^3$ as $r \rightarrow 0$, hence the P wave and S wave separately have a non-integrable singularity at $r = 0$, while their sum has an $1/r$ singularity Wu (1985), which is integrable. The refocused wavefields do not display this behaviour because these fields are source-free at $r = 0$, and therefore the wavefield is finite. Therefore, the P and S waves can be refocused separately without causing singularities, and the treatment given here is applicable to P , SV and SH waves separately.

The expressions above must be multiplied with the appropriate vector spherical harmonic (2)–(4) to obtain the full focused wavefield. For each wave type, a different spherical harmonic must be multiplied to characterize the wavefield. Additionally, in eqs (2)–(4), the vector spherical harmonics are summed over the angular order l and degree m which captures the imprint of the source properties

on each wave type. Therefore, each wave has its own dependence on the angles and on space and time.

If one were to use one component of the motion, such as the x -component, the source properties for the different wave types are superposed on each other. Since for a fixed source mechanism the radiation pattern of P and S waves are different, the focused wavefields do not provide clear information about the source mechanism. In order to avoid mixing of P - and S -radiated waves, one must decompose the wavefield using the divergence and curl in order to investigate the focus of each wave type (P and S) separately.

If one does not have a perfect aperture, a blurred focus will occur, and the focus cannot be characterized by one angular degree l but by the superposition of different angular degrees l . This applies to the spatial focus achieved in our numerical modelling.

NUMERICAL EXAMPLE

We illustrate the theory with a numerical example. We use the velocity model shown in the top panel of Fig. 1 to propagate the source wavefield to the receivers. The model consists of horizontally continuous layers whose P -wave velocities range from approximately 4.7 km s^{-1} to 5.9 km s^{-1} and S -wave velocities range from approximately 2.3 km s^{-1} to 2.9 km s^{-1} . In practice, one does not know the true velocity model. For this reason, we used the smoothed velocity model, shown in the bottom panel of Fig. 1, for the backpropagation.

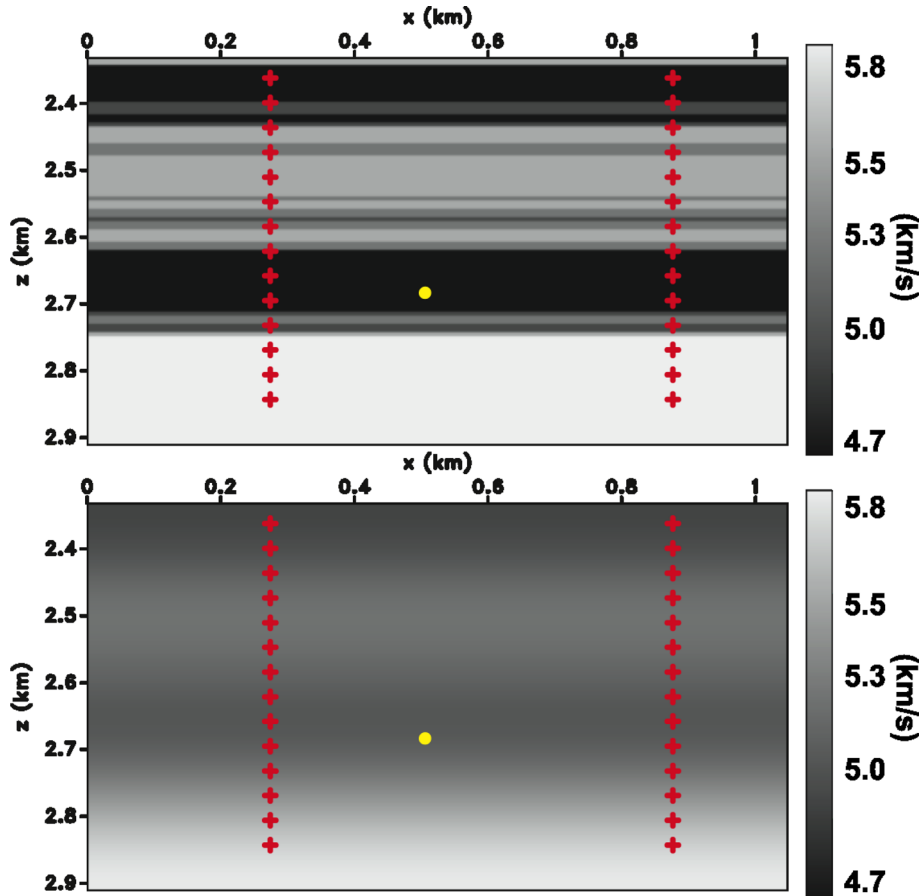


Figure 1. P -wave velocity models of the numerical experiment with units of km s^{-1} . Top panel indicates the correct velocity model and represents the velocity model used to propagate the source wavefield through the medium. Bottom panel indicates the smoothed velocity model with correct mean slowness. This model is used for backpropagation of the time-reversed signal and optimized inverse signal. The plus symbols represent the receivers, the circular dot represents the source. The S -wave velocity was the same but had velocities values equal to half of the P -wave velocity.

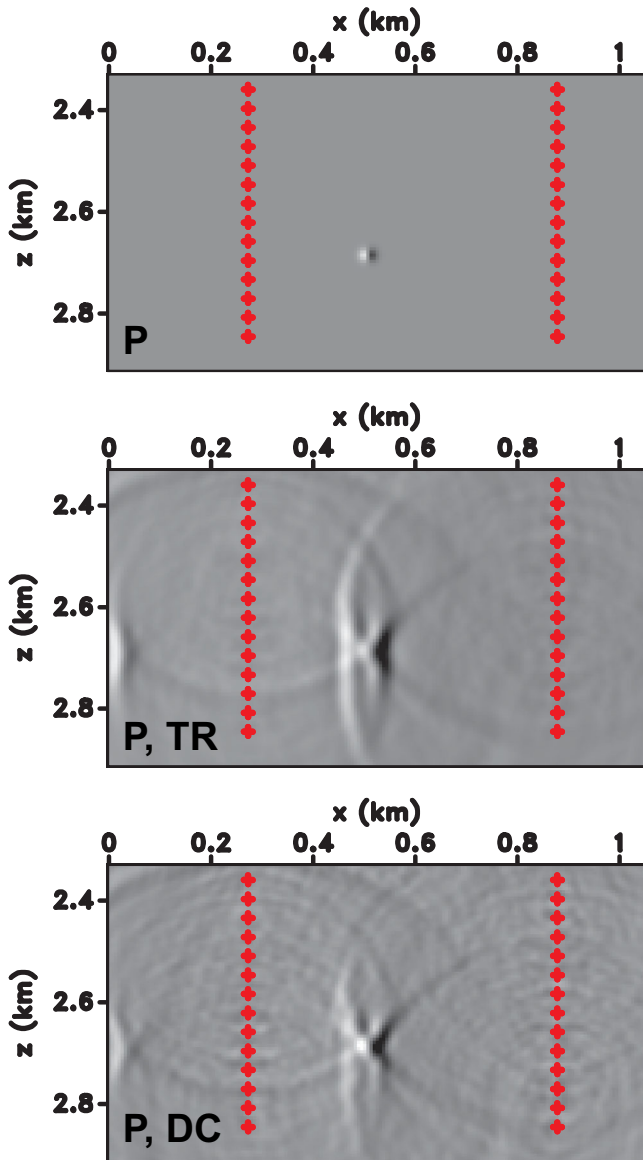


Figure 2. Decomposed P wavefield at time of focus due to horizontal point force. Top panel is P wave just after the horizontal point force is emitted. Middle panel indicates the result of injecting the time reversed signal back into the smoothed velocity model from the receiver locations. Bottom panel shows result of injecting the inverse signal calculated using deconvolution back into the smoothed velocity model from the receiver locations.

The velocity model is smoothed by using a 2-D triangle smoothing of the slowness with a smoothing radius of .185 km in the x and z directions (Fomel 2007). This smoothed velocity model has the same mean slowness as the correct velocity model.

We first use a horizontal point force located at $(x, z) = (0.51 \text{ km}, 2.68 \text{ km})$. The source is characterized by Ricker wavelet with dominant frequency of 100 Hz. There are 56 receivers distributed over two vertical boreholes in our model. The x -locations of the receiver boreholes are 0.74 km and 0.88 km, respectively. The receivers range from a depth of 2.36 km to 2.86 km with a spacing of 18.5 m.

In order to make the numerical simulation more realistic, we added bandpass limited noise to our recorded data at the receivers before applying time reversal or deconvolution. The additive noise only contains frequencies within the bandwidth of the data. We

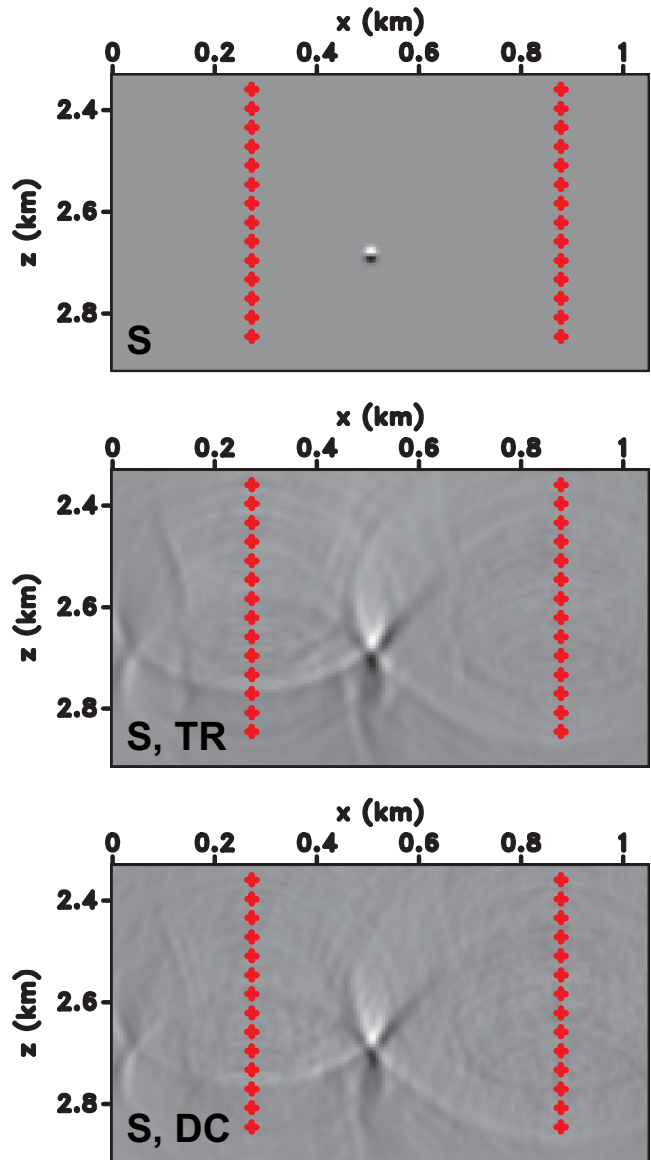


Figure 3. Decomposed S wavefield at time of focus due to horizontal point force. Top panel is S wave just after the horizontal point force is emitted. Middle panel indicates the result of injecting the time-reversed signal back into the smoothed velocity model from the receiver locations. Bottom panel shows result of injecting the inverse signal calculated using deconvolution back into the smoothed velocity model from the receiver locations.

calculated the energy ratio of the signal to noise, defined as the ratio of the sum of the signal and noise squared, to be equal to 0.89.

It is important to note that all the numerical work is done in-plane. The source wavefield propagates through our model. The vertical and horizontal displacement, which are recorded at the receiver locations, are oriented in-plane. When we solve for the S component by calculating the curl of the wavefield using the vertical and horizontal displacement, we imply that we are investigating the SV component. Therefore, we do not model the out of plane SH component. In this numerical example, sensors are deployed in two vertical boreholes. The theory presented here is, however, equally valid for a 2-D sensor network placed on, or near, the Earth's surface.

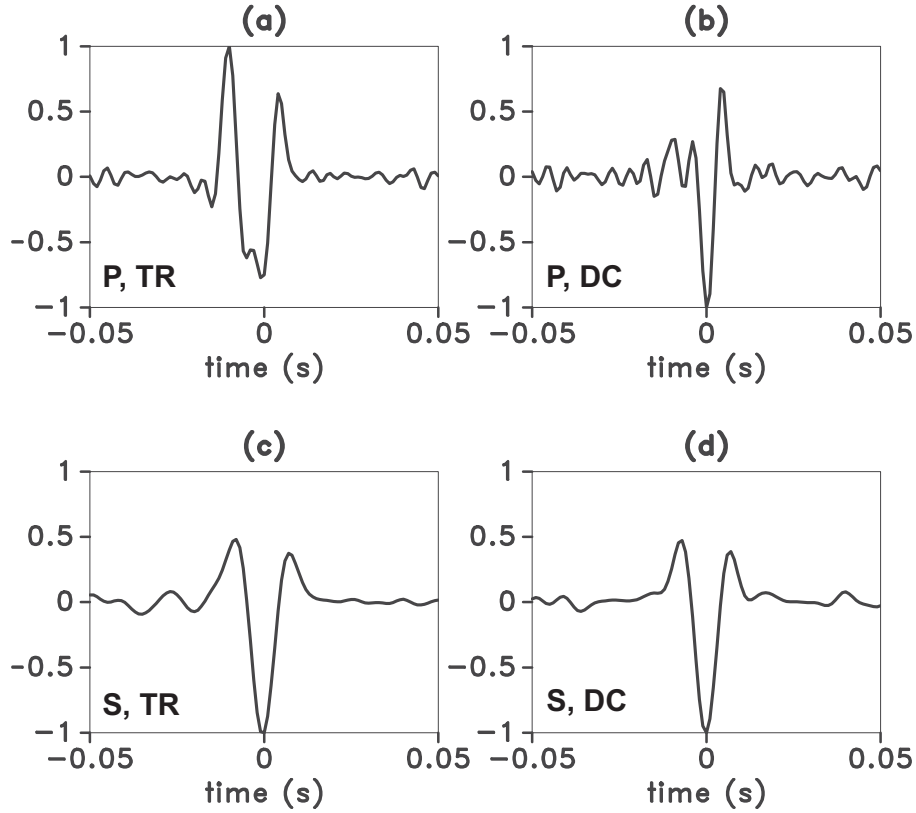


Figure 4. Temporal focused images due to a horizontal point force produced by backpropagating the calculated time-reversed signals using time reversal and deconvolution for vertical borehole array. Parts (a) and (b) are temporal focus of the P wave due to time reversal and deconvolution, respectively. Parts (c) and (d) are temporal focus of the S wave due to time reversal and deconvolution, respectively.

Horizontal point force

This section describes the numerical modelling that demonstrates that improved temporal focusing leads to improved spatial focusing for each wave type. We first model the wavefield due to a horizontal point force excitation at the source location. The horizontal and vertical displacements of the wavefield are then recorded at each receiver. Afterwards, we apply either time reversal or deconvolution to the recorded signals to generate the wavefields, which are backpropagated.

We use the time-reversed or deconvolved signals to excite waves that backpropagate through the smoothed velocity model, using the following forces acting at each of the receiver locations:

$$\vec{F}_{\text{TimeReverse}} = (U_x(-t), U_z(-t)), \quad (30)$$

$$\vec{F}_{\text{Deconv}} = (U_x^{\text{Inverse}}(t), U_z^{\text{Inverse}}(t)). \quad (31)$$

Here, $\vec{F}_{\text{TimeReverse}}$ and \vec{F}_{Deconv} are the source functions for time reversal and deconvolution, respectively, and $U_x(t)$ and $U_z(t)$ are the recorded signals. The inverse signal of a time-series $g(t)$ is defined as

$$g^{\text{inverse}}(t) \star g(t) = \delta(t), \quad (32)$$

where \star denotes convolution. In order to solve for $g^{\text{inverse}}(t)$ and avoid instability for $g^{\text{inverse}}(\omega)$ when $g(\omega) = 0$, we have to apply a water level regularization. Thus,

$$g^{\text{inverse}}(\omega) = \frac{1}{g(\omega)} \Rightarrow \frac{g^*(\omega)}{|g^*(\omega)|^2 + \epsilon}. \quad (33)$$

The derivation and explanation of these two methods are discussed in more detail by Douma *et al.* (2013).

After backpropagation, the wavefield is decomposed into P and S components for a crucial reason. We demonstrated in the ‘Theory’ section that improved temporal focusing leads to improved spatial focusing for each wave type. We do not consider the focus for the vertical or horizontal displacements. Rather, we use the displacement components to calculate the P and S wavefields using divergence and curl, respectively. This allows us to retrieve the P and S waves that have backpropagated from the sources. For each wave type, our theory predicts that an improved temporal focusing leads to improved spatial focusing.

We first model the wavefield due to a horizontal point force excitation at the source location. The top panel of Figs 2 and 3 show the P and S wavefields’ radiation pattern just after the horizontal point force is emitted and represent a pure angular degree $l = 1$. In perfect source imaging, we would reconstruct these radiation patterns. However, our aperture is not perfect and we backpropagate through a smoother version of the velocity model. Thus, we do not expect to be able to reconstruct these radiation patterns perfectly.

In order to show that deconvolution generates an improved spatial focus, we first demonstrate that deconvolution enhances the temporal focus. Thus, we calculate the temporal focusing for the P and S component as a result of deconvolution (eq. 31) compared with time reversal (eq. 30). We defined the temporal focusing in eq. (16) as the l -th derivative of the incoming wavefield. This is necessary because the wavefield is zero at our source location due of nodal lines. In order to demonstrate improved temporal focusing for a horizontal point force, we take the derivative of the P wavefield in the x -direction and the derivative of the S wavefield in the z -direction

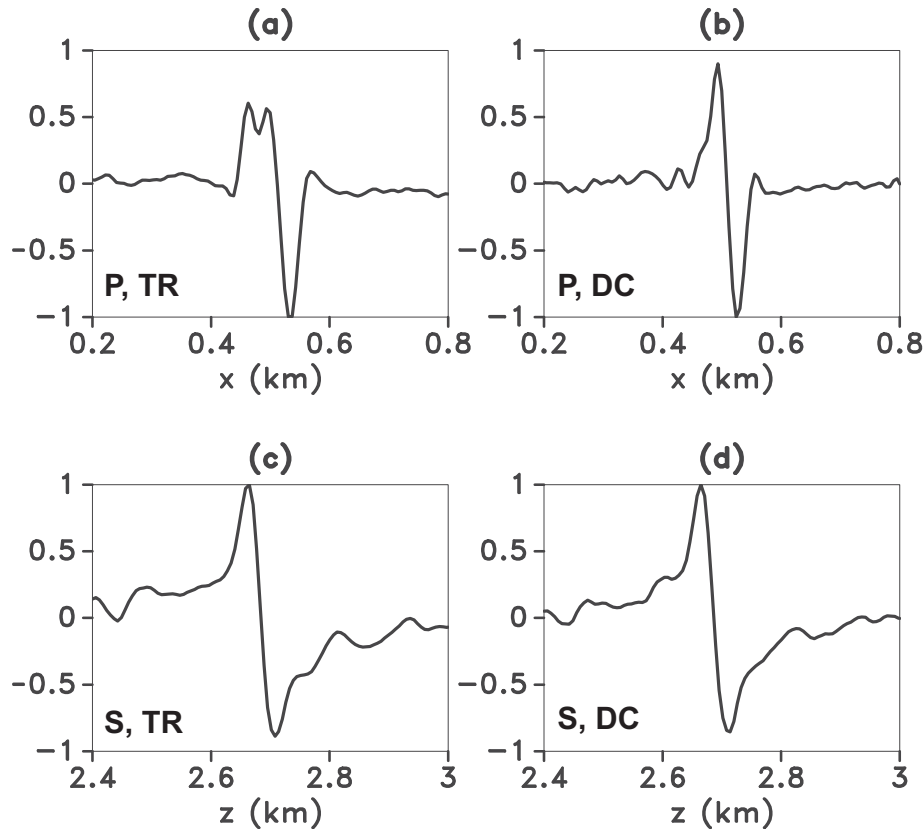


Figure 5. Spatial focused images due to a horizontal point force produced by backpropagating the calculated time-reversed signals using time reversal and deconvolution. Parts (a) and (b) are 1-D slices of Fig. 2 through depth 2.68 km. Parts (c) and (d) are 1-D slices of Fig. 3 through x location 0.51 km. Note the different scales used for the cross-section in the x and z direction.

because these derivatives are the radial derivatives perpendicular to the nodal lines for each wave type. We change the direction of the derivative because the radiation pattern of the P wave due to a horizontal point force is a dipole in the x -direction while the S -wave radiation has a dipole pattern oriented in the z -direction (Aki & Richards 2002). This is visible in the top panel of Figs 2 and 3, which show the radiation patterns of the P and S wavefields just after the source has acted. We calculate the derivatives as defined earlier to show the temporal focus for the P and S wave at the source location. Comparing Figs 4(a) to (b), one can clearly note that deconvolution has significantly improved the temporal focusing compared to time reversal for the P wave. In contrast, Figs 4(c) and (d) show that both time reversal and deconvolution produce a similar temporal focus for the S wave. Because improved temporal focusing implies better spatial focusing, see eq. (26), one would expect to see an improved spatial focus for the P wave using deconvolution compared to using time reversal. Additionally, we do not expect the S wave's spatial focus to improve using deconvolution because the temporal focus did not improve.

After having demonstrated that deconvolution improved the temporal focusing for the P wave, we compare the spatial focus generated by deconvolution and time reversal for each wave type. The backpropagated wavefields at $t = 0$ for the two methods are shown in the middle and bottom panels of Figs 2 and 3. The middle panel of Fig. 2 represents the spatial focus of the P wave using time reversal whereas the bottom panel shows the spatial focus of the P wave using time-reversal. Fig. 2 shows that deconvolution drastically improves the spatial focus compared to deconvolution. Fig. 3 does not show a clear improvement of spatial focusing between

time reversal (middle panel) and deconvolution (bottom panel) for the S component. This was expected due to deconvolution and time reversal producing similar temporal focuses for the S wave.

The aperture, over which we record the data that we backpropagate, is not perfect. This causes the spatial focuses, created using time reversal and deconvolution shown in Figs 2 and 3, to not be confined to one angular degree l because the spatial focuses are blurred in the z -direction. A perfect spatial focus would consist of only the $l = 1$ component. Figs 5(a, b) and (c, d) show cross-sections of the backpropagated wavefields in Figs 2 and 3 in the x - and z -directions, respectively, so that it is easier to assess the improvements and comparisons between the two methods. Note that the scales of the horizontal axis for Figs 5(a) and (b) are different from Figs 5(c) and (d). Fig. 5(a) demonstrates that time reversal is not able to create a well-defined dipole focus in the x -direction, which represents the radiation pattern of a P wave due to a horizontal point force. Fig. 5(b) shows that deconvolution is able to reconstruct the dipole radiation pattern of the P wave due to a horizontal point force. Figs 5(c) and (d) demonstrate that in this example there seems to be no significant difference between time reversal (c) and deconvolution (d) to reconstruct the S wave's focus.

Our numerical results have shown that deconvolution was able to improve the temporal focus for the P wave, which led to an improved reconstruction of the P wavefield's radiation pattern. However, deconvolution was not able to improve the temporal focus for the S -wave, due to a horizontal point force, which led to it also not improving the reconstruction of the S wavefield's radiation pattern. This can be attributed to the fact that a nodal line for the S wavefield's radiation pattern intersects the receiver array. Deconvolution

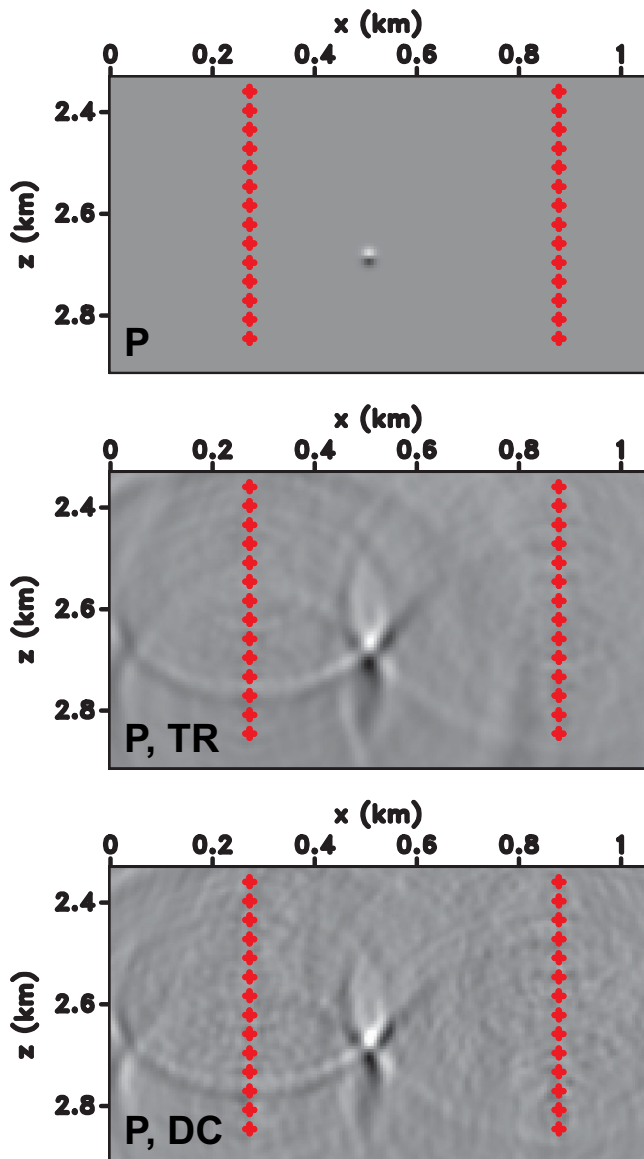


Figure 6. Decomposed P wavefield at time of focus due to vertical point force. Top panel is P wave just after the vertical point force is emitted. Middle panel indicates the result of injecting the time-reversed signal back into the smoothed velocity model from the receiver locations. Bottom panel shows result of injecting the inverse signal calculated using deconvolution back into the smoothed velocity model from the receiver locations.

assigns a larger weight to the receivers near the nodal line in order to increase a weak recorded signal. This is unphysical because there is no information to be gained in these weak recorded waveforms near the nodal lines. These receivers are supposed to record no information about the source and should, therefore, not propagate any information back. However, it simultaneously demonstrates the robust nature of deconvolution. For the radiation pattern which has a nodal line intersecting the receiver array, deconvolution does not generate an inaccurate but rather a comparable reconstruction of the radiation pattern as time reversal.

Vertical point force

We applied the same analysis towards a vertical point force using the same numerical model as for the horizontal point force. As pre-

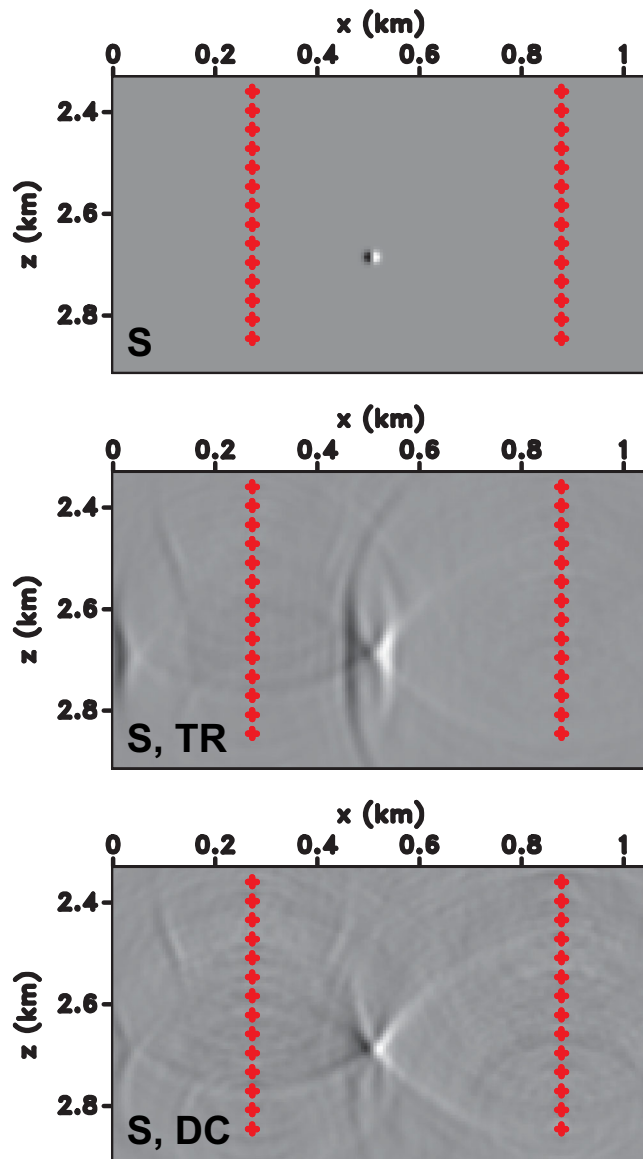


Figure 7. Decomposed S wavefield at time of focus due to vertical point force. Top panel is S wave just after the vertical point force is emitted. Middle panel indicates the result of injecting the time reversed signal back into the smoothed velocity model from the receiver locations. Bottom panel shows result of injecting the inverse signal calculated using deconvolution back into the smoothed velocity model from the receiver locations.

viously stated, the source wavelet was first injected into the correct velocity model at the source location. The horizontal and vertical displacements were then recorded at the receivers. Once these signals were recorded, time reversal and deconvolution methods were applied in order to calculate our backpropagating signals. These signals calculated using the two methods would then be propagate back into the smoothed velocity model from the receiver positions. We then decomposed the wavefield into the P and S component at the time of focus by taking the divergence and curl, respectively, of the displacements.

The top panels of Figs 6 and 7 show the P and S wavefield's radiation patterns after the vertical point force is emitted and represents the pure angular degree $l = 1$. As stated previously, one would be able to reconstruct the radiation patterns in perfect source imaging. However, we use the same numerical model as used for the hori-

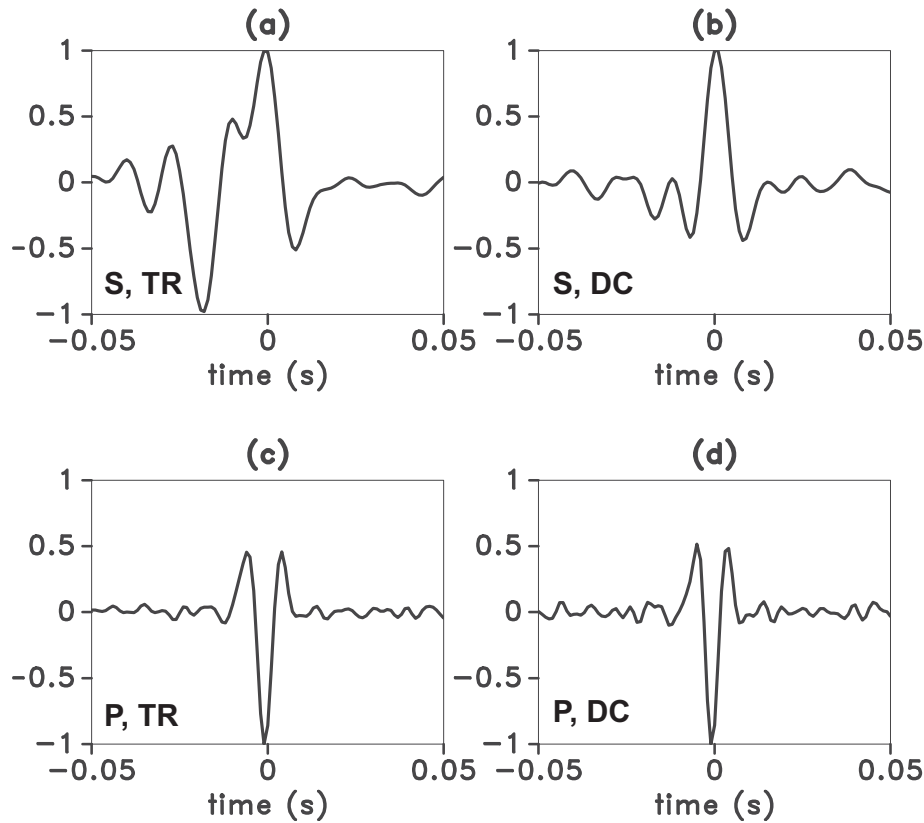


Figure 8. Temporal focused images due to a vertical point force produced by backpropagating the calculated time-reversed signals using time reversal and deconvolution for vertical borehole array. Parts (a) and (b) are temporal focus of the S wave due to time reversal and deconvolution, respectively. Parts (c) and (d) are temporal focus of the P wave due to time reversal and deconvolution, respectively.

zontal point force. Thus, we do not expect to be able to reconstruct the radiation patterns perfectly.

We first calculated the temporal focuses achieved using time reversal or deconvolution for the P and S components. Because the radiation patterns of the vertical point force are rotated 90° from the horizontal point force's, we take the derivative of the P wavefield in the z -direction and the derivative of the S wavefield in the x -direction in order to take the radial derivatives perpendicular to the nodal lines for each wave type. Comparing Figs 8(a) to (b), one can clearly note that deconvolution has significantly improved the temporal focusing compared to time reversal for the S wave; whereas, in Figs 8(c) and (d), time reversal and deconvolution produce a similar temporal focus for the P wave. Therefore, the results for the vertical point force are the reverse of that for the horizontal point force. This is expected as the radiation patterns are rotated by 90° , which cause the nodal lines to rotate. We have seen the impact of these nodal lines upon the focus we are able to achieve. As stated previously, because improved temporal focusing implies better spatial focusing, see eq. (26), one would expect to see an improved spatial focus now for the S wave using deconvolution compared to using time reversal. However, we do not expect to see any improvement in spatial focusing for the P component because deconvolution and time reversal generated comparable temporal foci for the P component.

Once shown that deconvolution improves the temporal focus for the S wave due to a vertical point force, we compare the spatial foci achieved using deconvolution or time reversal for both the P and S components. Figs 6 and 7 show the backpropagated wavefields

at $t = 0$ using either time reversal (middle panel) or deconvolution (bottom panel) for the P and S component, respectively. Fig. 7 shows that deconvolution significantly improves the spatial focus achieved for the S wave; Fig. 6 demonstrates that the spatial foci achieved for the P wave are comparable using either deconvolution or time reversal. These results were as expected because deconvolution improved the temporal focus for the S wave while generating a comparable temporal focus for the P wave.

In order to visualize the dipole foci achieved using either method, we generate 1-D slices through Figs 6 and 7. Figs 9(a) and (b) and (c) and (d) shows cross-sections of the backpropagated wavefields in Figs 2 and 3 in the x - and z -directions. Fig. 8(a) illustrates that time reversal is not able to create a well-defined dipole focus in the x -direction, which represents the radiation pattern of an S -wave due to a vertical point force. Fig. 9(b) shows that deconvolution is able to reconstruct the dipole radiation pattern of the S wave due to a vertical point force. Figs 9(c) and (d) demonstrate that there seems to be no significant difference between time reversal (c) and deconvolution (d) to reconstruct the P wave's focus. These results are a different way to illustrate what was shown in Figs 6 and 7.

Our numerical results for the vertical point force reiterate what we have seen in the horizontal point force results. We conclude that, for an elastic media without a perfect aperture and true velocity model, improved temporal focusing leads to improved spatial focusing. We have shown this both theoretically and numerically to be the case. Because deconvolution has the ability to improve the temporal focusing, one can improve the spatial focusing.

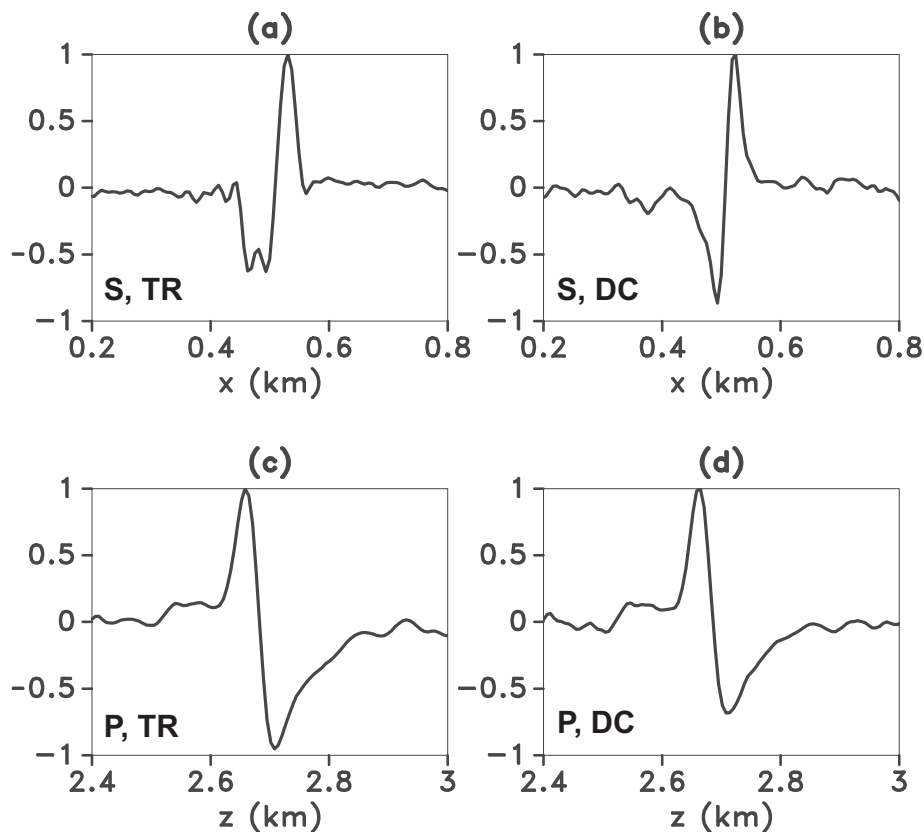


Figure 9. Spatial focused images due to a vertical point force produced by backpropagating the calculated time-reversed signals using time reversal and deconvolution. Parts (a) and (b) are 1-D slices of Fig. 2 through depth 2.68 km. Parts (c) and (d) are 1-D slices of Fig. 3 through x location 0.51 km. Note the different scales used for the cross-section in the x - and z -direction.

CONCLUSION

We have introduced deconvolution which improves the temporal focusing of microseismic events. The workflow for this approach is similar to imaging with time-reversed signals. The only difference is that instead of sending the time-reversed recorded signals into the medium, we send the inverse signal, as obtained by deconvolution, into the medium. The key result of this work is that we demonstrate theoretically and numerically that this improved temporal focusing leads to improved spatial focusing for each wave type in an elastic medium. This improved spatial focusing is beneficial for enhancing the focus of the elastic waves. The simplicity and robust nature of this method allows for a simple incorporation into existing reverse-time imaging methods. Additionally, the cost of deconvolution is minimal compared to running the finite difference modelling. Therefore, it can be added as a pre-processing step without significant additive cost.

REFERENCES

- Aki, K. & Richards, P., 2002. *Quantitative Seismology*, 2nd edn, Univ. Science Books.
- Anderson, B., Douma, J., Ulrich, T. & Snieder, R., 2014. Improving spatio-temporal focusing and source reconstruction through deconvolution, *Wave Motion*, doi:10.1016/j.wavemotio.2014.10.001.
- Arfken, G. & Weber, H., 2001. *Mathematical Methods for Physicists*, 5th edn, Harcourt.
- Artman, B., Podladtchikov, I. & Witten, B., 2010. Source location using time-reverse imaging, *Geophys. Prospect.*, **58**, 861–873.
- Aubry, J.-F., Tanter, M., Gerber, J., Thomas, J.-L. & Fink, M., 2001. Optimal focusing by spatio-temporal filter. II. Experiments. Application to focusing through absorbing and reverberating media, *J. acoust. Soc. Am.*, **110**, 48–58.
- Bancroft, J.C., Wong, J. & Han, L., 2010. Sensitivity measurements for locating microseismic events, *CSEG Recorder* (February), 28–37.
- Bertaix, V., Garson, J., Quieffin, N., Catheline, S., Derosny, J. & Fink, M., 2004. Time-reversal breaking of acoustic waves in a cavity, *Am. J. Phys.*, **72**(10), 1308–1311.
- Bose, S., Valero, H., Liu, Q., Shenoy, R.G. & Ounadjela, A., 2009. An automatic procedure to detect microseismic events embedded in high noise, *SEG Technical Program Expanded Abstracts*, pp. 1537–1541.
- Chapman, C., 2004. *Fundamentals of Seismic Wave Propagation*, Cambridge Univ. Press.
- Douma, J., Snieder, R., Fish, A. & Sava, P., 2013. Locating a microseismic event using deconvolution, *SEG Technical Program Expanded Abstracts*, pp.2206–2211.
- Duncan, P.M., 2005. Is there a future for passive seismic, *First Break*, **23**, 111–115.
- Fink, M., 1997. Time reversed acoustics, *Phys. Today*, **50**(3), 34–40.
- Fomel, S., 2007. Shaping regularization in geophysical-estimation problems, *Geophysics*, **72**(2), R29–R36.
- Foulger, G.R. & Julian, B.R., 2012. Earthquakes and errors: methods for industrial applications, *Geophysics*, **76**(6), WC5–WC15.
- Gallot, T., Catheline, S., Roux, P. & Campillo, M., 2011. A passive inverse filter for Green's function retrieval, *J. acoust. Soc. Am.*, **131**, EL21–EL27.

- Hayles, K., Horine, R.L., Checkles, S., Blangy, J.P. & Corporation, H., 2011. Comparison of microseismic results from the Bakken Formation processed by three different companies: integration with surface seismic and pumping data, *SEG Technical Program Expanded Abstracts*, pp. 1468–1472.
- Jonsson, B.L.G., Gustafsson, M., Weston, V.H. & Hoop, M.V.D., 2004. Retrofocusing of acoustic wave fields by iterated time reversal, *SIAM J. appl. Math.*, **64**(6), 1954–1986.
- Kendall, M., Maxwell, S., Foulger, G., Eisner, L. & Lawrence, Z., 2011. Special section microseismicity: beyond dots in a box introduction, *Geophysics*, **76**(6), WC1–WC33.
- Kummerow, J., 2010. Using the value of the crosscorrelation coefficient to locate microseismic events, *Geophysics*, **75**(4), MA47–MA52.
- Larmat, C., Montagner, J., Fink, M., Capdeville, Y., Tourin, A. & Clévéde, E., 2006. Time-reversal imaging of seismic sources and application to the great Sumatra earthquake, *Geophys. Res. Lett.*, **33**, L19312, doi:10.1029/2006GL02636.
- Larmat, C., Guyer, R. & Johnson, P., 2010. Time-reversal methods in geophysics, *Phys. Today*, **63**(8), 31–35.
- Lu, R., 2008. *Time Reversed Acoustics and Applications to Earthquake Location and Salt Dome Flank Imaging*, Massachusetts Institute of Technology. Earth Resources Laboratory.
- Lu, R., Toksöz, M.N. & Willis, M.E., 2008. Locating microseismic events with time reversed acoustics: a synthetic case study, *SEG Technical Program Expanded Abstracts*, pp. 1342–1346.
- Montaldo, G., Tanter, M. & Fink, M., 2004. Real time inverse filter focusing through iterative time reversal, *J. acoust. Soc. Am.*, **115**, 768–775.
- Parvulescu, A., 1961. Signal detection in a multipath medium by M.E.S.S. processing, *J. acoust. Soc. Am.*, **33**, 1674–1674.
- Roux, P. & Fink, M., 2000. Time reversal in a waveguide: study of the temporal and spatial focusing, *J. acoust. Soc. Am.*, **107**, 2418–2429.
- Song, F., Kuleli, H.S., Toksöz, M.N., Ay, E. & Zhang, H., 2010. An improved method for hydrofracture-induced microseismic event detection and phase picking, *Geophysics*, **75**(6), A47–A52.
- Steiner, B., Saenger, E.H. & Schmalholz, S.M., 2008. Time reverse modeling of low-frequency microtremors: application to hydrocarbon reservoir localization, *Geophys. Res. Lett.*, **35**(3), L03307, doi:10.1029/2007GL032097.
- Tanter, M., Thomas, J.-L. & Fink, M., 2000. Time reversal and the inverse filter, *J. acoust. Soc. Am.*, **108**, 223–234.
- Tanter, M., Aubry, J.-F., Gerber, J., Thomas, J.-L. & Fink, M., 2001. Optimal focusing by spatio-temporal filter. I. Basic principles, *J. acoust. Soc. Am.*, **110**, 37–47.
- Vignon, F., Aubry, J.-F., Saez, A., Tanter, M., Cassereau, D., Montaldo, G. & Fink, M., 2006. The Stokes relations linking time reversal and the inverse filter, *J. acoust. Soc. Am.*, **119**, 1335–1346.
- Wu, R.S. & Ben-Menahem, A., 1985. The elastodynamic near field, *Geophys. J. R. astr. Soc.*, **81**, 609–622.

APPENDIX: DETAILS OF THE DERIVATION

In this appendix, we derive an equation representing the spatial focusing in an elastic medium and demonstrate that has improved temporal focusing implies improved spatial focusing for each wave type.

We assume that the incoming wave $f_i(t)$ at angular degree l of expression (10) is given and first show how this function constrains the Fourier coefficient $A_l(\omega)$ in eq. (9). The incoming wave is, in the frequency domain, given by

$$\begin{aligned} U_l^{\text{inc}}(r, \omega) &= \frac{1}{2\pi} \int \frac{f_i(t+r/c)}{r} e^{i\omega t} dt = \frac{e^{-i\omega r/c}}{r} \frac{1}{2\pi} \int f_i(t) e^{i\omega t} dt \\ &= \frac{e^{-i\omega r/c}}{r} F_l(\omega), \end{aligned} \quad (\text{A1})$$

where the replacement $t \rightarrow t - r/c$ is used in the second identity, and $F_l(\omega)$ is the incoming wave in the frequency domain. Because expressions (10) and (A1) only hold in the limit $r \rightarrow \infty$, we proceed by analysing eq. (9) in the same limit where, according to eq. (11.158) of Arfken & Weber (2001), the spherical Bessel functions are given by

$$\begin{aligned} j_l(kr) &= \frac{\sin(kr - l\pi/2)}{kr} \\ &= (-i)^{l+1} \frac{e^{ikr}}{2kr} + i^{l+1} \frac{e^{-ikr}}{2kr} \quad \text{as } r \rightarrow \infty. \end{aligned} \quad (\text{A2})$$

The last term gives the incoming wave. Therefore, the incoming wave component of the spherical Bessel function at large distances r is given by $j_l^{\text{inc}}(kr) = i^{l+1} e^{-ikr}/2kr$ ($r \rightarrow \infty$). Using this in expression (8) and equating it with eq. (A1) gives:

$$\frac{e^{-i\omega r/c}}{r} F_l(\omega) = i^{l+1} \frac{e^{-i\omega r/c}}{2kr} A_l(\omega) \quad \text{as } r \rightarrow \infty. \quad (\text{A3})$$

The r -dependence is the same on the left-hand side and the right-hand side of this equation. Eq. (A3) can be solved to give $A_l(\omega) = (-i)^{l+1} (2\omega/c) F_l(\omega)$. Inserting this into expression (9) leads to eq. (11). This expression relates the total wavefield to the Fourier transform of the incoming wavefield. Note that this expression is valid for all values of r . The limit $r \rightarrow \infty$ was only used to relate $A_l(\omega)$ to the incoming wave. In practice, one can evaluate expression (A3) for a large radius $\omega r/c \gg 1$, and one does not need to take the limit $r \rightarrow \infty$.

The factor $(-i\omega)$ corresponds in the time domain to differentiation. In the following, we will apply repeated differentiations and integrations. For this reason we employ the notation shown in eqs (12) and (13). Note that a negative value of n corresponds to an integration. With this notation, expression (11) can be written as

$$u_l(r, t) = (-i)^l \frac{2}{c} \int F_l^{(1)}(\omega) j_l(kr) e^{-i\omega t} d\omega. \quad (\text{A4})$$

The total wavefield (A4) can also be related to the incoming wave in the time domain. In order to derive this, we use expression (11.165) of Arfken & Weber (2001) to express the spherical Bessel function of order l into the spherical Bessel function of order 0:

$$\begin{aligned} j_l(x) &= (-x)^l \left(\frac{1}{x} \frac{d}{dx} \right)^l j_0(x), \text{ hence} \\ j_l(kr) &= (-1)^l \frac{r^l}{k^l} \left(\frac{1}{r} \frac{d}{dr} \right)^l j_0(kr). \end{aligned} \quad (\text{A5})$$

Using eq. (A4) and the relation $k = \omega/c$ in eq. (A5) gives

$$u_l(r, t) = 2r^l c^{l-1} \left(\frac{1}{r} \frac{d}{dr} \right)^l \int \frac{F_l^{(1)}(\omega)}{(-i\omega)^l} j_0(kr) e^{-i\omega t} d\omega. \quad (\text{A6})$$

Because of definition (13), $F_l^{(-1)}(\omega)/(-i\omega)^l = F_l^{(1-l)}(\omega)$, and we can simplify eq. (A6) to

$$u_l(r, t) = 2r^l c^{l-1} \left(\frac{1}{r} \frac{d}{dr} \right)^l \int F_l^{(1-l)}(\omega) j_0(kr) e^{-i\omega t} d\omega. \quad (\text{A7})$$

The reason we relate $u_l(r, t)$ to the spherical Bessel function of order 0 is that this allows us to carry out the Fourier transform analytically. In order to do this, we use expression (11.148) of Arfken & Weber (2001)

$$j_0(kr) = \frac{\sin kr}{kr} = \frac{c}{2i\omega r} (e^{i\omega r/c} - e^{-i\omega r/c}), \quad (\text{A8})$$

where we use $k = \omega/c$ in the last identity. Using this result, the integral in eq. (A7) becomes

$$\begin{aligned} & \int F_l^{(1-l)}(\omega) j_0(kr) e^{-i\omega t} d\omega \\ &= -\frac{c}{2r} \int F_l^{(-l)}(\omega) (e^{-i\omega(t-r/c)} - e^{-i\omega(t+r/c)}) d\omega \\ &= \frac{c}{2r} (f_l^{(-l)}(t+r/c) - f_l^{(-l)}(t-r/c)), \end{aligned} \quad (\text{A9})$$

where expression (A8) was used in the first identity. Inserting eq. (A9) into eq. (A7) gives eq. (14). This expression gives an explicit relation between the total wavefield for all values of r and the incident wave at great distance.

In order to determine the temporal focus (16), we need to evaluate $d^l j_l(kr)/dr^l$. According to eq. (11.144) of Arfken & Weber (2001),

$$j_l(x) = \frac{2^l l!}{(2l+1)!} x^l + O(x^{l+2}) \quad \text{as } x \rightarrow 0. \quad (\text{A10})$$

Using that $(d/dr)^l r^l = l!$, we get

$$\lim_{r \rightarrow 0} \frac{d^l}{dr^l} j_l(kr) = b_l k^l = b_l \omega^l / c^l, \quad (\text{A11})$$

where b_l is given by eq. (18). Combining eqs (16), (A4), and (A11) gives the following expression for the temporal focus

$$T_l(t) = \frac{2b_l}{c^{l+1}} \int (-i\omega)^l F_l^{(1)}(\omega) e^{-i\omega t} d\omega. \quad (\text{A12})$$

With the definition (11), this can be rewritten as

$$T_l(t) = \frac{2b_l}{c^{l+1}} \int F_l^{(l+1)}(\omega) e^{-i\omega t} d\omega. \quad (\text{A13})$$

Therefore, after taking the Fourier integral, we found a relationship between the temporal focus and the incoming wavefield.